Preprint Cambridge Centre for Computational Chemical Engineering ISSN 1473 – 4273

# Numerical simulation and parametric sensitivity study of particle size distributions in a burner-stabilised stagnation flame

Edward K. Y. Yapp[1], Dongping Chen[1], Jethro Akroyd[1], Sebastian Mosbach[1], Markus Kraft[1,2], Hai Wang[3]

Draft of November 14, 2014

[1] Department of Chemical Engineering
and Biotechnology
University of Cambridge
New Museums Site
Pembroke Street
Cambridge, CB2 3RA
United Kingdom
E-mail: mk306@cam.ac.uk

[2] School of Chemical
and Biomedical Engineering
Nanyang Technological University
62 Nanyang Drive
Singapore 637459

[3] Department of Mechanical Engineering
Stanford University
Stanford, California 94305
E-mail: haiwang@stanford.edu

Preprint No. 148


*Keywords:* Soot, Particle size distribution, Premixed flame, Numerical simulation, Parametric sensitivity study, PAH

**Edited by**
Computational Modelling Group
Department of Chemical Engineering and Biotechnology
University of Cambridge
New Museums Site
Pembroke Street
Cambridge CB2 3RA
United Kingdom

**Fax:** + 44 (0)1223 334796
**E-Mail:** c4e@cam.ac.uk
**World Wide Web:** http://como.cheng.cam.ac.uk/

## Highlights

- Detailed population balance model used to perform a parametric sensitivity study
- Soot morphology and its effect on the interpretation of mobility size measurements


### Abstract

A detailed population balance model is used to perform a parametric sensitivity study on the computed particle size distributions (PSDs) for a laminar premixed ethylene burner-stabilised stagnation flame. The soot morphology in the post-flame region is studied using computed sintering level distributions, fringe length analysis of the polycyclic aromatic hydrocarbons within the primary soot particles, and TEM-like projections of aggregates. The computed PSDs were found to be most sensitive to the minimum particle inception size, the coagulation rate and the inception species concentration. The PSDs were generally insensitive to the other parameters in the population balance model. Changes in the particle inception size and the coagulation rate led to an overall shift in the position of the coagulation peak. Only changes in the inception species concentration led to a systematic shift in both the position of the trough between the modes of the bimodal PSD and the coagulation peak at larger diameters. Given the overall model, varying the inception species concentration with each burner-stagnation plate separation was the only means possible to achieve a satisfactory agreement between the experimental and computed PSDs and soot volume fractions. This study shows that further work is required to better understand the soot precursor chemistry, the inception of soot particles. Additional work may also be needed in the area of experimental mobility sizing for the flame studied here.


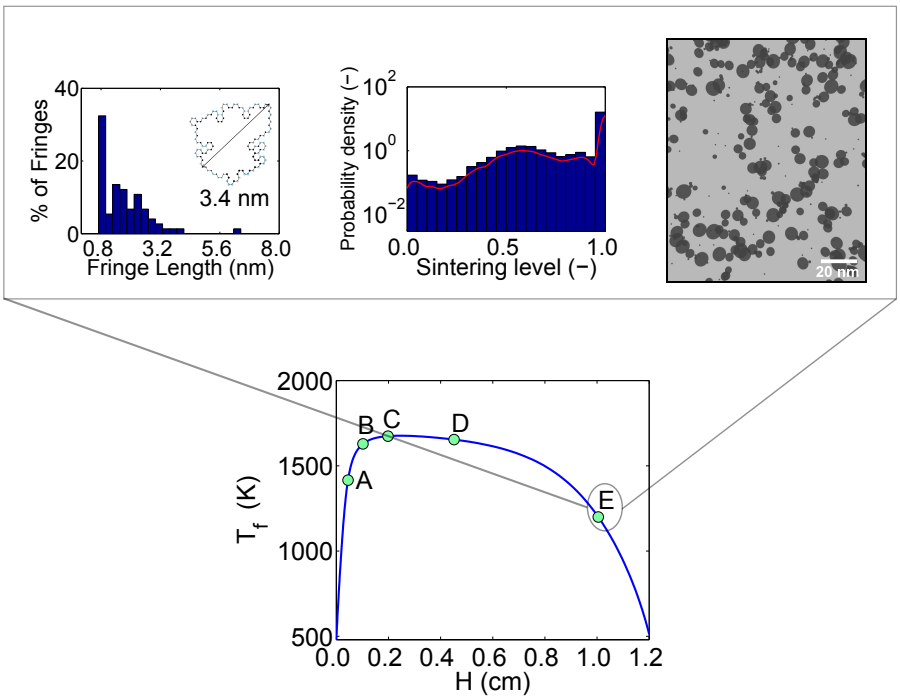

# Contents

# 1 Introduction

Much progress has been made to understand the chemical and physical processes underlying soot formation. However, details of the individual processes remain an open question [13, 68]. In general, a basic understanding of the complex and often competitive processes of soot nucleation and mass/size growth requires detailed kinetic modeling through comparison of model results and experimental data and sensitivity analysis. For this purpose, a range of experimental techniques have been developed to probe the size and mass evolution of soot in flames. Soot volume fraction is most commonly measured using light extinction and scattering [12] and laser light incandescence [59]. However, interpretation of the laser-based experiment requires a fairly precise knowledge about the refractive index of young soot which remains poorly understood. In principle, independent verification of the optical measurements may be made using small-angle neutron scattering [71], small-angle X-ray scattering [26] and thermocouple particle densitometry [38], though very little systematic efforts have been made in that direction. The detailed distribution of particle sizes may be measured by a scanning mobility particle sizer (SMPS) (see, e.g., [36, 37, 58, 75–77]). Though the method is intrusive to the flame, it nonetheless provides more detailed features about the evolution of the particle size distribution (PSD), from very small, incipient particles to aggregates as large as 100 nm in mobility diameter. Ex situ analysis by high-resolution microcopy of particles collected by a rapid insertion technique has been routinely employed (see, e.g., [16, 28, 48, 55]). Whilst transmission electron microscopy (TEM) images show the morphology of a soot particle, the higher magnification (see, e.g., [66]) is able to reveal some details of the internal structure of mature soot. Imaging incipient soot a few nanometers in size by TEM is challenging [77], because of potential sample damage by the vacuum environment and the high-energy electron beam of TEM, as shown recently by Schenk et al. [55]. Recent advances in Helium ion microscopy (HIM) offer a low-energy, softer and high-contrast solution to incipient soot imaging [55, 56]. The chemical composition of soot may be analysed using laser microprobe spectroscopy [15, 16] and photoionisation aerosol mass spectroscopy [45].

A large portion of the experimental data that are available with regards to the time evolution of soot PSD has been gathered in premixed flames [2, 3, 45, 58, 74–77]. A sample probe is typically placed across the flame and PSDs would be measured by a SMPS. This sampling technique is inherently intrusive and perturbs the flame [14, 75]. For this reason, a premixed burner-stabilised stagnation flame (BSSF) configuration was introduced where the sample probe is integrated into a water-cooled stagnation plate as a flow stagnation surface for which pseudo-one-dimensional numerical solution of the flame problem becomes feasible [4]. The probe in that setup may be treated as the flame boundary condition; thus, eliminating the problem in earlier setups in which the probe effects on fluid mechanics and reaction kinetics cannot be quantified easily. The setup, along with the numerical modeling method for such flames, removes the need to carry out arbitrary "time or spatial distance shifting" as it was customarily employed in comparison of experimental data and modelling result.

Beyond the probe effect, measurements by SMPS coupled with BSSF faces other complications when such measurements are used for testing models. Like any other techniques

for probing soot in flames, the interpretation of the data is not always straightforward. Mobility measurements yields essentially the collision diameter of the particles. Thus two factors can impact a proper comparison between model and experiment. The first factor lies in the unknown morphology of the particles undergoing mass and size growth. The second factor is related to the internal structure of the particles and thus the mass density of the particle. HIM measurements have shown that particles < 10 nm in size can exhibit odd, non-spherical shapes. Considering the experimental issues just discussed, it would be beneficial to carry out a study in which the model and experimental uncertainties are considered jointly. This paper will be a step in that direction.

The soot PSDs for an ethylene BSSF were modelled by Lindstedt and Waldheim [34] using a surface volume description of particles and a sectional method. To counteract the excessive depletion of the small particles in their model, they introduced a collision efficiency for coagulation which varies between 1 for particle diameters greater than 5 nm and about 0.01 for pyrene. However, there are still some unresolved problems. For example, the model is unable to predict particle diameters across all burner-stagnation plate separations. It remains unclear whether the discrepancy is caused by the particle morphological assumptions of the model in the simulation or by other factors.

There are also many detailed models of soot formation and solution methods [39]. For example, Kraft and co-workers [9, 10, 40, 49–51, 54] employ a detailed population balance model which is solved using a stochastic method. The model has an unprecedented level of chemical and physical details, giving insight into particle size, morphology, and the internal structure of nanoparticles. This particular modelling approach has been successfully applied to the analysis of a variety of nanoparticles. It was used to simulate the PSDs of soot particles in laminar premixed flames [43, 62, 74] and to uncover the various factors that govern the shape of PSDs and their time evolution [62, 74]. Specifically, Singh et al. [62] performed a sensitivity analysis of the PSDs to various kinetic parameters in the hydrogen-abstraction–carbon addition (HACA) mechanism [20]. A unique feature of the model is that it resolves the size and connectivity of the primary particles in an aggregate; therefore, TEM-like projections of aggregates could be produced to visualise the temporal evolution of the fractal dimension in different flames [43]. Similar investigations of soot PSDs, morphology and composition have been performed in the context of engines [44]. The stochastic approach was also used to follow the morphology of aerosols in Titan's atmosphere [30] and to study the sintering of titania [73], silica [53] and silicon [41]. One has to be aware, though, that the increasing complexity of the model comes at a cost of including a large number of parameters, some of which were calibrated against experiments, while others remain poorly known.

The **purpose of this paper** is to investigate whether the model can describe the evolution of soot PSDs observed in the BSSF of Abid et al. [4]. The flame chemistry and structure was computed using a pseudo-one-dimensional stagnation flow flame code with appropriate boundary conditions. The particle dynamics were solved using a detailed population balance model. A thorough parametric sensitivity study is carried out here to understand how the various submodels and model parameters impact the various PSD features quantitatively and to shed light on the mobility measurement, especially concerning the particle morphology and its effect on the interpretation of the mobility diameter.

The paper is organised as follows: Section 2 introduces the gas-phase chemical mecha-

nism, the governing equations and boundary conditions for the burner-stagnation flame configuration, and key aspects of the detailed population balance model. Sections 3.1 and 3.2 present the temperature and species profiles, and the PSDs. Section 3.3 presents the parametric sensitivity study of the computed PSDs. Section 3.4 shows various aspects of the soot morphology calculated from the detailed population balance model.

# 2 Computational method

The computational method consists of two parts. In the first part, temperature and species profiles are computed using a modified version [4] of Oppdif [35, 63], including calculation of the source terms by the Method of Moment with Interpolative Closure (MOMIC) using the code published by Revzan et al. [52]. A gas-phase chemical mechanism, and species thermodynamic and transport properties are supplied as input. The transport equations of the moments of the PSD are solved to approximately account for the production and consumption of key gas-phase species due to surface growth, oxidation and condensation processes. A total of six moments, including the zeroth moment, were solved using MOMIC to close the moment transport equations. In the second part, a detailed population balance model is applied as a post-processing step where the computed temperature and species profiles from Oppdif are supplied as input. This two-step methodology has been applied to the studies of a number of laminar premixed flames [11, 46, 61] and ideal reactor simulations [5].

Oppdif simulations were performed using a unburned-gas composition (molar basis) of 16.3 % ethylene, 23.7 % oxygen and 60 % argon (an equivalence ratio of 2.07), a cold gas velocity of 8 cm/s (STP), a burner temperature of 473 K and at atmospheric pressure, in accordance with the experimental conditions [4]. Windward differencing was used and multi-component transport and thermal diffusion were considered. About 200 grid points were found to be sufficient for convergence. The energy equation was solved with both gas and particle radiation.

The detailed population balance model requires the computed profiles from Oppdif to be expressed in terms of the residence time of a Lagrangian particle travelling from the burner to the stagnation plate. The combined axial convective velocity and thermophoretic velocity were used to perform the conversion as per Abid et al. [4].

## 2.1 Gas-phase chemistry

The ABF mechanism [6] as supplied with the Chemkin-Pro installation package [1] was used to describe the gas-phase chemistry. The reaction mechanism is an extension of the model described in Wang and Frenklach [69] and includes combustion chemistry and the formation and growth pathways of polycyclic aromatic hydrocarbons (PAHs) up to pyrene [69] and additional PAH growth reactions added by Appel et al. [6].

## 2.2 Governing equations and boundary conditions

The complete set of governing equations and boundary conditions are stated for the BSSF shown in **Fig**. 1. The motivation for this is that there are certain inconsistencies in the formulation of the moment transport equation where the variation in density in the diffusion term is neglected [1, 70]. Furthermore, the moment boundary conditions are not well-documented.

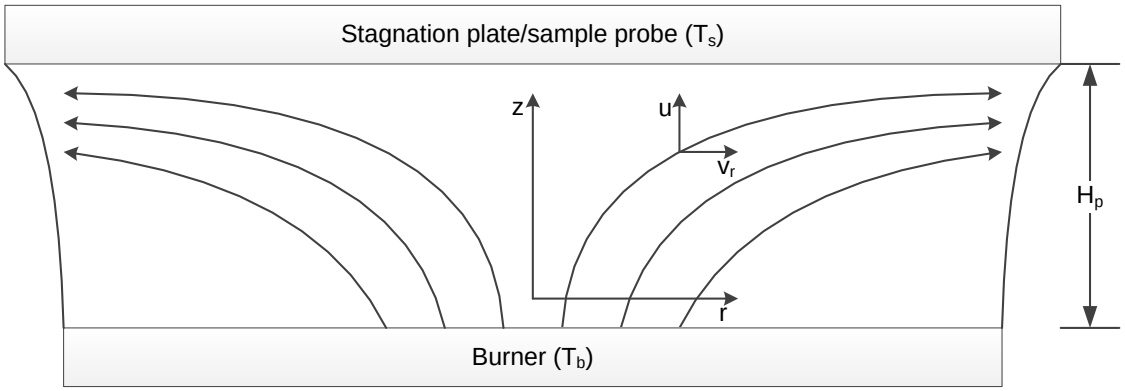


**Figure 1:** *Illustration of the coordinate system and the flow field in the burner-stabilised stagnation flame configuration. $T$ is the temperature, $H_\mathrm{p}$ is the burner-stagnation plate separation, and $u$ and $v_\mathrm{r}$ are the axial and radial velocities in the $z$ and $r$ directions, respectively.*

By assuming that the radial velocity varies linearly in the radial direction, the governing equations for the 2D axisymmetric flow field may be reduced to a set of 1D equations given below [27, 47, 63]:

**Continuity equation**

$$\frac{\mathrm{d}F}{\mathrm{d}z} - G = 0, \tag{1}$$

with

$$F = \frac{\rho u}{2}, \quad G = -\frac{\rho v_r}{r}, \tag{2}$$

where $\rho$ is the density, and $u$ and $v_\mathrm{r}$ are the axial and radial velocities in the $z$ and $r$ directions, respectively.

**Radial momentum equation**

$$\Lambda - 2\frac{\mathrm{d}}{\mathrm{d}z}\left(\frac{FG}{\rho}\right) + \frac{3G^2}{\rho} + \frac{\mathrm{d}}{\mathrm{d}z}\left[\mu\frac{\mathrm{d}}{\mathrm{d}z}\left(\frac{G}{\rho}\right)\right] = 0, \tag{3}$$

where $\mu$ is the dynamic viscosity.

**Radial pressure gradient eigenvalue, $\Lambda$**

$$\Lambda - \frac{1}{r}\frac{\partial p}{\partial r} = 0, \tag{4}$$

where $p$ is the pressure.

**Species equation**

$$2F\frac{\mathrm{d}Y_k}{\mathrm{d}z} + \frac{\mathrm{d}}{\mathrm{d}z}(\rho Y_k V_k) - \dot{\omega}_k W_k = 0, \quad k = 1,\ldots,N, \tag{5}$$

where the multicomponent diffusion velocity of the $k$-th gas-phase species is:

$$V_k = \frac{1}{X_k \bar{W}} \sum_{j\neq k}^{N} W_j D_{k,j} \frac{\mathrm{d}X_j}{\mathrm{d}z} - \frac{D_{\mathrm{T},k}}{\rho Y_k}\frac{1}{T}\frac{\mathrm{d}T}{\mathrm{d}z}. \tag{6}$$

$Y_k$ is the mass fraction, $X_k$ is the mole fraction, $\dot{\omega}_k$ is the molar chemical rate of production per unit volume, $W_k$ is the molecular weight, and $D_{k,j}$ and $D_{\mathrm{T},k}$ are the molecular and thermal diffusion coefficients of the $k$-th gas-phase species. $\bar{W}$ is the mean molecular weight of the mixture and $N$ is the number of gas-phase species.

**Energy equation**

$$2F\frac{\mathrm{d}T}{\mathrm{d}z} - \frac{1}{c_\mathrm{p}}\frac{\mathrm{d}}{\mathrm{d}z}\left(\lambda\frac{\mathrm{d}T}{\mathrm{d}z}\right) + \frac{\rho}{c_\mathrm{p}}\sum_{k=1}^{N} c_{\mathrm{p},k} Y_k V_k \frac{\mathrm{d}T}{\mathrm{d}z} + \frac{1}{c_\mathrm{p}}\sum_{k=1}^{N} h_k \dot{\omega}_k + \frac{1}{c_\mathrm{p}}\dot{Q}_\mathrm{rad} = 0, \tag{7}$$

where $T$ is the temperature, $c_\mathrm{p}$ is the specific heat capacity at constant pressure of the mixture, $c_{\mathrm{p},k}$ is the specific heat capacity at constant pressure of the $k$-th gas-phase species, $\lambda$ is the thermal conductivity and $h$ is the molar enthalpy.

Heat loss due to gas and particle radiation in the optically-thin limit is [60]:

$$\dot{Q}_\mathrm{rad} = 4\sigma(T^4 - T_\mathrm{amb}^4)\left(\sum_{k}^{N} p(X_k a_k) + \kappa_\mathrm{particle}\right), \tag{8}$$

where $\sigma$ is the Stefan-Boltzmann constant, $T_\mathrm{amb}$ is the ambient temperature taken to be the average of the burner and stagnation plate temperatures [4], and $a_k$ and $\kappa$ are the Planck mean absorption coefficients of the $k$-th gas-phase species and soot particle, respectively. Details of the gas radiation model may be found in ref. [4]. The Planck mean absorption coefficient of the particle may be expressed as [42]:

$$\kappa_\mathrm{particle} = 3.83 f_\mathrm{v} C_0 T / C_2, \quad C_0 = \frac{36\pi nk}{(n^2 - k^2 + 2)^2 + 4n^2k^2}, \tag{9}$$

where $f_v$ is the soot volume fraction. $C_0 = 4.8922$ (dimensionless) is a constant depending on the complex refractive index of soot, where $n = 1.57$ and $k = 0.56$ are the refractive and absorptive indices, respectively [64]. $C_2 = 1.4388$ cm K is the second Planck function constant.

**Moment transport equation**

$$2F\frac{\partial}{\partial z}\left(\frac{M_r}{\rho}\right) - \frac{\partial}{\partial z}\left[\rho D_{\mathrm{p},1}\frac{\partial}{\partial z}\left(\frac{M_{r-2/3}}{\rho}\right)\right] + \frac{\partial v_{\mathrm{T}} M_r}{\partial z} - \dot{M}_r = 0, \quad r = 0,\ldots,\infty, \tag{10}$$

where the moments of the size distribution of particles are defined as [19]:

$$M_r = \sum_{i=1}^{\infty} i^r N_i, \quad r = 0,\ldots,\infty. \tag{11}$$

The $\dot{M}_r$ term in Eq. 10 is the moment source term as contributed by inception, coagulation, surface growth, oxidation and condensation [18, 19, 21]. Inception is assumed to occur by the dimerisation of two pyrene molecules producing a new particle that contains 32 carbon atoms. Particles are subjected to a size-dependent collision rate [18] and undergo surface growth reactions described by the HACA mechanism [20] and oxidation by $O_2$ and OH [21]. Pyrene was assumed to be the only condensation species.

The diffusion coefficient of a particle of size 1 is [23]:

$$D_{\mathrm{p},1} = \frac{3}{2\rho}\left(1 + \frac{\pi\alpha_{\mathrm{T}}}{8}\right)^{-1}\left(\frac{\bar{W}k_{\mathrm{B}}T}{2\pi N_{\mathrm{A}}}\right)^{1/2}\frac{1}{d_1^2}, \tag{12}$$

where $\alpha_{\mathrm{T}}$ is the thermal accommodation factor which represents the equilibrium fraction of gas molecules that leave the particle surface and is usually near 0.9 [23]. $k_{\mathrm{B}}$ is the Boltzmann constant, $N_{\mathrm{A}}$ is the Avogadro constant and $d$ is the diameter.

The thermophoretic velocity may be expressed as [67]:

$$v_{\mathrm{T}} = -\frac{3}{4}\left(1 + \frac{\pi\alpha_{\mathrm{T}}}{8}\right)^{-1}\frac{\mu}{\rho T}\frac{\mathrm{d}T}{\mathrm{d}z}. \tag{13}$$

A generalised theory for the transport of nano-sized particles was advanced by Li and Wang [31–33] where the transition from diffuse to specular scattering and van der Waals gas-particle interaction were accounted for. The influence of the improved diffusion and thermophoretic terms is to be investigated in future.

**Boundary conditions**

$$z = 0: \quad F = \frac{\rho_{\mathrm{b}} u_{\mathrm{b}}}{2},\ G = 0,\ T = T_{\mathrm{b}},\ \rho Y_k V_k = \rho u_{\mathrm{b}}(Y_{k,\mathrm{b}} - Y_k), \tag{14}$$

$$M_r = 0, \tag{15}$$

where the value of $F$ at the burner is based on the density and velocity of the feed. $G$ is zero because the radial velocity at the burner is assumed to be 0. $T_\mathrm{b}$ is the burner temperature and the species specification allows diffusion back into the burner.

$$z = H_\mathrm{p}: \quad F = 0,\ G = 0,\ T = T_\mathrm{s},\ \rho Y_k V_k = 0, \tag{16}$$

$$\frac{\partial \nu_\mathrm{T} M_r}{\partial z} - \frac{\partial}{\partial z}\left[\rho D_{\mathrm{p},1} \frac{\partial}{\partial z}\left(\frac{M_{r-2/3}}{\rho}\right)\right] = 0, \tag{17}$$

where $H_\mathrm{p}$ is the burner-stagnation plate separation, $T_\mathrm{s}$ is the plate temperature, and the boundary conditions for $F$, $G$ and $Y$ follow from a non-slip condition assumed at the plate.

**Overall problem**

The overall problem may be stated as seeking the solution to $\mathbf{f}(\phi) = 0$ where $\mathbf{f}(\phi)$ is a residual function formed by the left-hand sides of Eqs. 1, 3, 4, 5, 7 and 10, subject to the boundary conditions in Eqs. 14 to 17. The dependent variable vector is:

$$\phi = (F, G, \Lambda, Y_k, T, M_r).$$

It may be noted that Oppdif implements modified versions of Eqs. 10, 15 and 17 to solve for the natural logarithm of the moments because the values of the different moments may vary by several orders of magnitude. The moment boundary condition at the plate (Eq. 17) was found to be well-approximated by a zero-gradient as there was no significant difference in the steady-state solution. It also resulted in a significant improvement in the convergence of the solution.

## 2.3 Detailed population balance model

A detailed population balance model [11] was used to model soot formation by postprocessing the Oppdif simulations of the BSSF. The growth of PAH species within the model is described by a kinetic Monte-Carlo-aromatic site (KMC-ARS) model [49], starting from pyrene. The dynamics of the soot particle population is described by the Smoluchowski equation [23, 24, 57] with additional terms for particle inception, surface growth, oxidation, condensation and sintering. A detailed description of the particle model [11, 49, 54] and the stochastic numerical method used to simulate the population dynamics [8, 46] may be found elsewhere. A brief description of the most important aspects of the particle model is given below.

In the model, soot particles are represented as aggregates composed of primary particles, where each primary particle is composed of a number of PAHs [54]. A PAH is represented by the number of carbon and hydrogen atoms it contains, and the number and types of elementary sites on its edge [49]. These elementary sites include free-edge, zig-zag, armchair and bay sites [9, 17]. This representation allows the exact structure and fringe length (defined as the largest carbon-carbon pair distance) of each individual PAH to be resolved. A primary particle is represented as a set of two or more PAHs. An aggregate is represented as a set of two or more primary particles. Each aggregate stores a list of neighbouring

primary particles and resolves the shared surface area between each pair of neighbours, where each pair of neighbours can be in point contact, can be fully coalesced or can be anywhere in between [54]. The level of coalescence is described by a *sintering level* [53]. A sintering level of 0 corresponds to point contact and a sintering level of 1 corresponds to complete coalescence.

There are five different particle processes in the model:

**Inception** A primary particle is formed when two PAH molecules stick following a collision. The sticking probability of these two PAHs is determined by a simple collision efficiency model [11]. If the sum of the masses of the collision partners exceeds a given threshold, then they will stick. This implies a unity sticking probability.

**Coagulation** An aggregate is formed when two (primary or aggregate) particles stick following a collision. The rate of collision is determined by a transition regime coagulation kernel [46] which is dependent on the mass and collision diameter of each collision partner. After a coagulation event, two primary particles (one from each collision partner) are assumed to be in point contact. These primaries may undergo subsequent particle rounding due to mass addition [54] via surface growth and condensation, and due to sintering [53].

**Surface growth** PAHs in a primary particle may grow via surface reactions with gas-phase species. The rate of surface growth is a function of the structure of the PAH and is described by the KMC-ARS model. Two parameters are introduced to differentiate the rate of growth of PAHs in a primary particle versus those in the gas phase. The *growth factor* $g \in [0,1]$ [54] is a multiplier that is applied to the growth rate of PAHs within primary particles where the number of PAHs exceeds a critical number of PAHs, $n_{\text{crit}}$. It is intended to account for the possibility that PAHs in large primary particles grow more slowly than PAHs in the gas-phase.

Surface growth increases the mass of a PAH, which results in an increase in the sphericity of the primary particle containing the PAH and any neighbouring primary particles [54]. This particle rounding takes the form of an increase in the shared surface area between the affected primary particles. The rate of particle rounding is parameterised by a smoothing factor $s \in [0,2]$ [54] that relates the change of the shared surface area to the change of the volume of a primary particle. A smoothing factor of 0 implies instantaneous coalescence, whereas a smoothing factor of 2 corresponds to no rounding.

**Condensation** PAHs in a primary particle may grow via condensation of a gas-phase PAH, following a collision between the PAH and a primary or aggregate particle. The rate of collision is calculated as per coagulation, except that one of the collision partners is a molecule. Rounding by mass addition occurs via the same mechanism as described for the surface growth process above.

**Sintering** Neighbouring primary particles may undergo particle rounding via a sintering process. The rate of sintering between each pair of neighbouring primary particles

$p_i$ and $p_j$ is given [53]:

$$\frac{\mathrm{d}C_{i,j}}{\mathrm{d}t} = -\frac{1}{\tau_\mathrm{s}}(C_{i,j} - S_{i,j}), \tag{18}$$

where $C_{i,j}$ is the shared surface area of primary particles $p_i$ and $p_j$, and $S_{i,j}$ is the surface area of a sphere with the same volume as primaries $p_i$ and $p_j$. The characteristic sintering time is given [65]:

$$\tau_\mathrm{s} = A d_{i,j} \exp\left[\frac{E}{T}\left(1 - \frac{d_\mathrm{crit}}{d_{i,j}}\right)\right], \tag{19}$$

where $A$ is the pre-exponential factor, $d_{i,j}$ is the minimum diameter of two neighbouring primary particles, $E$ is the activation energy and $d_\mathrm{crit}$ is the critical diameter for sintering. For $d_{i,j} < d_\mathrm{crit}$, sintering is assumed to be instantaneous.

The sintering level $c_{i,j}$ determines how far primary particles $p_i$ and $p_j$ have sintered:

$$c_{i,j} = \frac{\frac{S_{i,j}}{C_{i,j}} - 2^{-1/3}}{1 - 2^{-1/3}}, \tag{20}$$

where a value of 1 implies that the primary particles are in point contact, while a value of 0 means that the primary particles are fully sintered.

There are many parameters in the model, but the key parameters investigated in this work are shown in **Table** 1. Ranges within which these parameters are expected to vary and the initial values chosen for the base case simulations are shown. A threshold of 32 carbons in the collision efficiency model means that pyrene molecules or larger are assumed to stick upon collision. The five parameters $\rho$, $s$, $g$, $E$ and $d_\mathrm{crit}$ were optimised by Chen et al. [11] in a two-step process against the experimental PSDs for a set of laminar premixed ethylene flames [25].

**Table 1:** *Model parameters in detailed population balance model.*

| Parameter (units) | Range | Value |
|---|---|---|
| 1) Collision efficiency model: | | |
| - Threshold (number of carbons) | $\geq 12$ | 32 |
| 2) Soot density, $\rho$ ($\mathrm{g\,cm^{-3}}$) | $1 \leq \rho \leq 2$ | 1.4 |
| 3) Smoothing factor, $s$ (-) | $0 \leq s \leq 2$ | 1.69 |
| 4) Growth factor, $g$ (-) | $0 \leq g \leq 1$ | 0.0263 |
| 5) Critical number of PAHs in a primary particle before the growth factor is applied, $n_\mathrm{crit}$ (-) | $\geq 2$ | 50 |
| 6) Sintering model: | | |
| - $A$ ($\mathrm{s\,m^{-1}}$) | N/A | $1.1 \times 10^{-14}$ |
| - $E$ (K) | $1.8 \times 10^4 \leq E \leq 1.8 \times 10^5$ | $9.61 \times 10^4$ |
| - $d_\mathrm{crit}$ (nm) | $1 \leq d_\mathrm{crit} \leq 5$ | 1.58 |

# 3 Results and discussion

## 3.1 Temperature and species profiles

The centerline temperature for the stagnation flame in **Fig**. 2 was measured using a coated thermocouple [4] as a function of height above burner surface, $H$ for six burner-stagnation plate separations, $H_p$ = 0.55, 0.6, 0.7, 0.8, 1.0 and 1.2 cm. The top panel of Fig. 2 shows a comparison of the experimental and computed temperature profile for the largest burner-stagnation plate separation, $H_p$ = 1.2 cm. The results are similar for the other separations. The size of the experimental error bars is due to the uncertainty (50 – 100 %) in the emissivity of the thermocouple coating [4]. Also shown in Fig. 2 (bottom panel) is a comparison of the maximum flame temperature for a range of separations. The maximum flame temperature increases with increasing separation due to the reduced conductive heat transfer to the stagnation plate as the burner to stagnation surface separation increases. Clearly the temperatures computed using the ABF model (solid lines) in the flame and postflame regions are as much as 150 K lower than the experimental value; and in the preheat zone the rise of the experimental temperature is slower than the computed results.

Previously, the same flame was simulated using USC Mech II [72]. The results show close agreement between the experimental and simulated temperature profiles for all $H_p$ values. These simulations are repeated here with results also shown in Fig. 2. The inability of the ABF model to reproduce the temperature was puzzling initially, but it became clear to us that the flame chemistry part of the model over-predicts the laminar flame speed over the entire range of equivalence ratio, by as much as 30 cm/s (or over 100%) at the equivalence ratio of 1.8. The significantly larger flame speed leads to a faster rise in the temperature in the preheat zone and a greater heat loss to the burner. The result is a significantly reduced maximum flame temperature as seen in Fig. 2. The discrepancy of the experimental and simulated temperature is discerning, especially considering that the rate of soot formation is expected to be dependent on the temperature. As will be discussed later, we have carried out simulations both by solving the energy equation and by imposing the experimental temperature on the OPPDIF calculations. The difference in results will be discussed in detail.

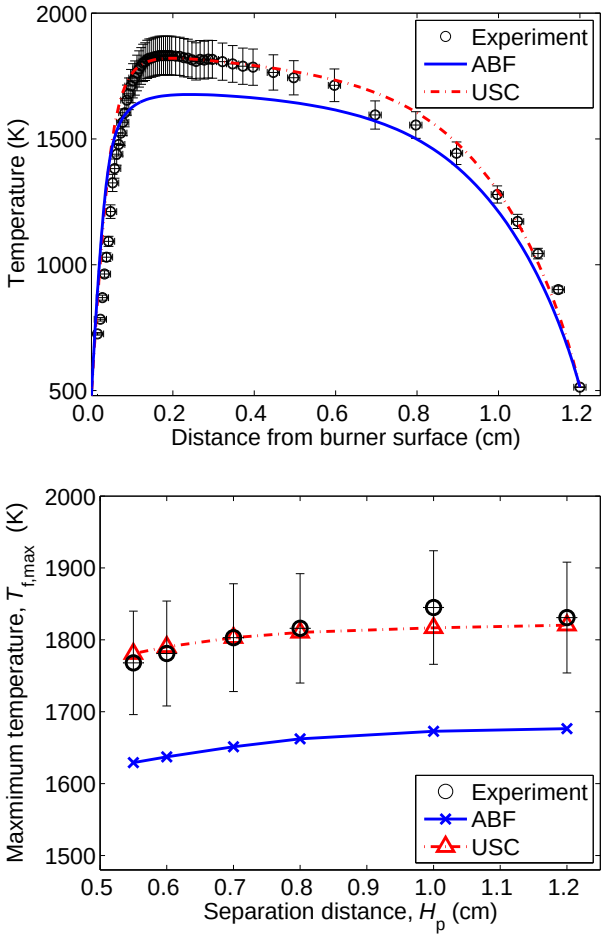


**Figure 2:** *Top panel: Comparison of experimental (symbols) and computed (solid line: ABF model; dashed-dotted-dashed line: USC Mech II) centerline temperature profiles for a burner-stagnation plate separation of 1.2 cm. Bottom panel: Comparison of experimental (symbols) and computed (solid line through symbols: ABF model; dashed-dotted-dashed line through symbols: USC Mech II) maximum flame temperatures at several burner-stagnation plate separations.*

Over almost the entire range of spatial distance of the post-flame region, the concentrations of the major species are nearly constant, as shown in **Fig**. 3 for $H_p$ = 1.2 cm as an example, except for $H_2$, which drops notably towards the stagnation surface. This is caused by the Soret effect: the sharp temperature gradient near the surface draws in heavier species. By continuity, the light species, e.g., $H_2$, must have a reduced concentration to compensate for the enrichment of the heavy species, as evidenced by the slight upward bending of the $CO_2$ mole fraction curve towards the stagnation surface. Figure 3 also shows major species profiles computed by imposing the experimental temperature profile without solving the energy equation. Overall, the temperature discrepancy causes small, but notable changes in the major species profiles.

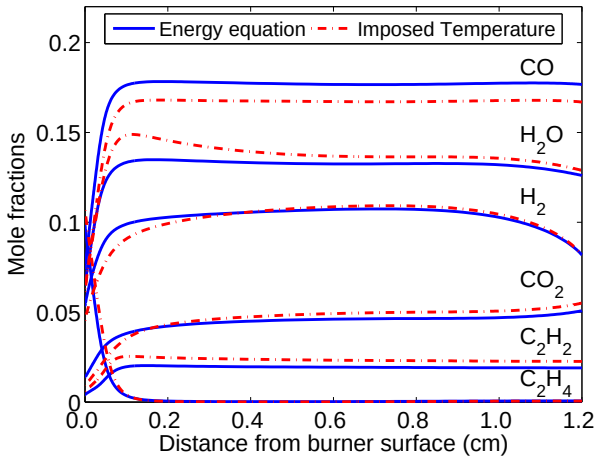


**Figure 3:** *Typical main species profiles computed for a burner-stagnation plate separation of 1.2 cm. Solid line: ABF model with energy equation solved; dashed-dotted-dashed lines: ABF model with experimental temperature profiles imposed.*

Hydrogen atoms are critical to radical site generation in PAH molecules and soot surfaces [70]. **Figure** 4 shows the H atom, benzene and pyrene mole fraction profiles computed for a range of burner-stagnation plate separations. All three profiles show that the flames are very similar up to about 0.2 cm above the burner surface. The length of the post-flame region increases with increasing burner-stagnation plate separation.

Zhao et al. [76] showed that in high temperature flames ($T_{f,max}$ > 1850 K), computed benzene profiles would initially rise, then fall in the post-flame region; whereas, in low temperature flames ($T_{f,max}$ < 1850 K), the benzene concentration would continue to rise in the post-flame region. The rise-then-fall behaviour has been explained to be the competition of PAH mass growth [69] and thermal decomposition [22]. We do not see the rise-then-fall in the benzene profiles here because these are a set of low temperature flames. However, we see a rise-then-fall in the profiles of pyrene because of its consumption from particle inception and condensation on soot surfaces.

The discrepancy for the temperature prediction by the base model has a notable impact on the H atom concentration and the prediction of precursors to soot. **Figure** 5 shows a comparison of the computed H atom and pyrene profiles where the energy equation was solved and where the experimental temperature profile was imposed at $H_p$ = 1.2 cm.

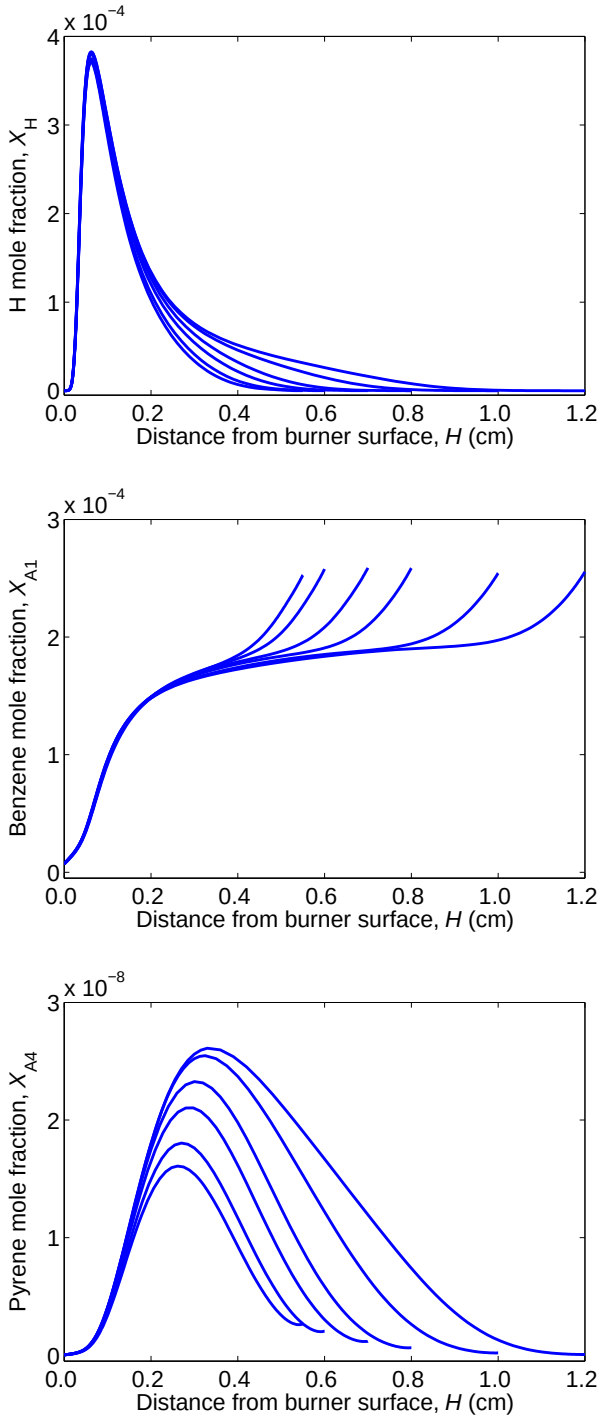


**Figure 4:** *Hydrogen atom, benzene and pyrene mole fraction profiles computed using the ABF model by solving the energy and other conservation equations for several burner-stagnation plate separations, which are indicated by the value of H at the end of each curve.*

The higher temperatures imposed increases the H atom and peak pyrene concentration; however, it lowers the pyrene concentration in the post-flame region, for reasons to be

discussed later.

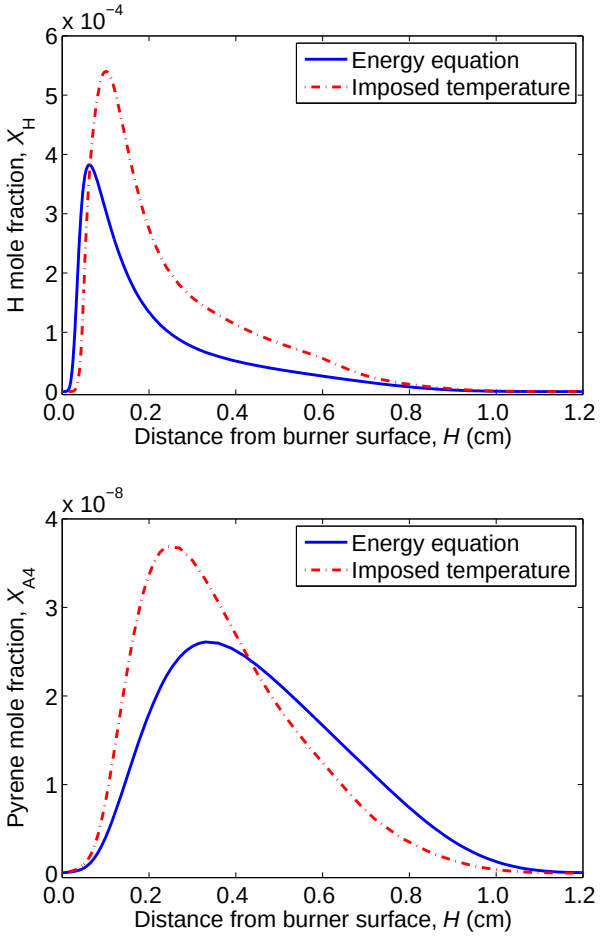


**Figure 5:** *Comparison of computed hydrogen atom (top panel) and pyrene (bottom panel) profiles where the energy equation was solved using the ABF model (with gas and particle radiation correction) and where the experimental temperature profile was imposed, both for a burner-stagnation plate separation of 1.2 cm.*

## 3.2 Particle size distributions

PSDs were determined by mobility diameter measurements and later compared with the particle sizes determined by HIM [55, 56]. The inability to fully reconcile the PSDs highlights the need to model the mobility diameter which may aid in the interpretation of the mobility measurements. While it is assumed that the mobility diameter is equal to the collision diameter the question remains as how the collision diameter should be defined. Our model's ability to distinguish between PAHs, primary particles and aggregates allows us to apply varying definitions of the collision diameter depending on the different "types" of particles.

**PAHs and Primary particles**

The collision diameter is assumed here as:

$$d_c = \max\left(\left(\frac{6V}{\pi}\right)^{1/3}, \left(\frac{2n_c}{3}\right)^{1/2}\right), \tag{21}$$

where the first term in the parenthesis corresponds to the equivalent spherical diameter while the second term corresponds to Frenklach's geometric relationship for the most condensed PAH series [21]. $V$ is the "volume" of the PAH (or PAHs in the case of primary particles) calculated from the total mass of carbon and hydrogen atoms, and the density of soot material. $n_c$ corresponds to the number of carbon atoms in a PAH. In light of the unknown mass density of the soot material when the particles are merely clusters of a few PAHs and the known non-sphericity of the primary particles, we expect Eq. 21 to be over-simplified - an issue to be discussed later.

**Aggregates**

The collision diameter follows the form of Kruis et al. [29]:

$$d_c = d_p n_p^{1/D_f} = \frac{6V}{A}\left(\frac{A^3}{36\pi V^2}\right)^{1/D_f} = \frac{6}{(36\pi)^{1/D_f}}\frac{V^{1-2D_f}}{A^{3/D_f-1}}, \tag{22}$$

where $d_p$ is the average primary particle diameter, $n_p$ is the average number of primary particles in the aggregate, and $D_f$ is the fractal dimension of soot particles (= 1.8). Note that in the case of surface-volume models [7] which assume monodisperse, spherical primary particles in point contact, $d_p$ and $n_p$ represent the real primary particle diameter and number, respectively.

$A$ is the surface area of the aggregate:

$$A = \frac{A_{sph}}{c_{avg}(1-n^{-1/3})+n^{-1/3}}, \tag{23}$$

where $A_{sph}$ is the equivalent spherical surface area, $c_{avg}$ is the average sintering level of the particle, and $n$ is the number of primary particles. $c_{avg}$ is calculated as the summation of all pairwise sintering levels in the particle (Eq. 20) and averaged across the number of primary particle connectivities (or $n-1$). Equation 23 interpolates between the surface

area of a spherical particle ($c_{avg} = 1$) and the surface area of a particle where the primary particles are in point contact ($c_{avg} = 0$).

The predicted PSDs are found to be in qualitative agreement with the experimental data. In particular, the base case calculation yields the bimodal distribution as observed experimentally. Quantitatively, however, the PSDs differ notably. There are three key aspects in the disagreement, as shown in Figure 6. First, the base case simulation yields onset of particle nucleation earlier than the experimental counterpart. For $H_p$ = 0.55 cm, the experiment shows the first burst of small particles entering into the lower cutoff size of 2.5 nm, but computationally the model predicts substantially larger particles. Despite the earlier nucleation, however, the model predicts a smaller size growth rate. For example, at $H_p$ = 1.2 cm, the model underpredicts the mean diameter of the large-size mode of particles by as much as a factor of 2. Lastly, the trough separating the two size modes was predicted to be deeper and smaller than the experiment. A similar finding with a different modelling approach has been reported previously [34].

The discrepancy observed above is not entirely the consequence of temperature. As shown in Fig. 6, imposing the experimental temperature profile leads to an increase in the particle size as compared to the base case simulation. The increase in the predicted particle size is caused, to an extent, by the increased peak pyrene concentration, as seen in Fig. 5. Likewise, the larger soot surface area also leads to greater rates of pyrene consumption and a lowered pyrene consumption in the post flame. Overall, neither the base case simulation nor the run with imposed temperature reproduces the PSD data well. In what follows, we shall carry out sensitivity analysis on the various model parameters to understand the plausible cause for the discrepancy.

## 3.3 Parametric sensitivity study

Key features of a bimodal PSD are identified for the purpose of making quantitative comparisons between the experimental and computed PSDs. **Figure** 7 shows these features: (a) a mode at small diameters (the inception peak) which represents incipient particles, (b) a mode at larger diameters (the coagulation peak) which represents particles that have grown by coagulation and surface growth, (c) a trough between these two modes and (d) the "largest" particle. Each feature has an associated number density and particle diameter $D_p$. Following the approach of Singh et al. [62], the diameter of the "largest" particle is defined to be the greatest diameter for which $\mathrm{d}N/\mathrm{d}\log(D_p) = 0.01N_{total}$, where $N_{total}$ is the total number density. $N_{total}$ is based on particle diameters $D_p > 2.5$ nm as the particle detection limit of the SMPS is 2.5 nm [4].

Key model parameters considered for sensitivity analysis are (a) the minimum particle inception size, (b) the particle-particle coagulation rate and (c) the pyrene concentration. The computation is carried out for $H_p$ = 1.2 cm. **Figure** 8 shows the results of varying: (a) the minimum particle inception size, (b) the coagulation rate and (c) the pyrene concentration at $H_p$ = 1.2 cm. To eliminate the uncertainty associated with the temperature prediction, the experimental temperature profile was imposed. The computed PSDs were generally insensitive to the other parameters in Table 1. Similar results were found for all other burner-stagnation plate separations ($H_p$ = 0.55, 0.6, 0.7, 0.8 and 1.0 cm). The

minimum particle inception size was varied from 32 carbons (base case) to 1024 carbons, and a constant multiplicative factor of 2, 4 and 8 was applied to the coagulation kernel to assess the effect of changing the coagulation rate. In either case, there is no systematic shift in the position of the trough, as shown in Fig. 8; however, there is an overall shift in the position of the coagulation peak to larger diameters. Increasing the minimum particle inception size increases the average size of PAHs in a particle. On the other hand, increasing the coagulation rate increases the number of coagulation events and therefore the number of PAHs in a particle. Both effects lead to an increase in particle diameter. A constant pyrene profile, i.e., the pyrene concentration does not change with height above burner, was imposed to understand the effect of precursor concentration on the various PSD features. Increasing the pyrene concentration leads to a systematic shift in both the position of the trough and the position of the coagulation peak to larger diameters, leading to a better agreement between the experimental and computed PSDs. Hence, it appears that the trough position is related to the precursor concentration or nucleation strength. The result here highlights the importance of precursor concentration in predicting the qualitative PSD features.

## 3.4 Soot morphology

**Figure** 9 shows various aspects of the soot morphology calculated from the detailed population balance model: (a) the evolution of the structure and fringe length of a representative PAH along the flame (top panel) and (b) computed fringe length distributions, sintering level distributions and computed, quasi-TEM images (bottom panel) in the post-flame region. The fringe length distribution corresponds to an aggregate which contains the largest (the number of carbon atoms) PAH at that point in the flame. The sintering level was calculated as an average for each aggregate in the particle ensemble and a distribution of these values are shown. In the TEM images, aggregates are represented as spheres in point contact.

Point D is a high temperature region just behind the flame front. The sintering level distribution and quasi-TEM image show that inception is dominant and almost all the particles in the ensemble are spherical. Point E is at a lower temperature near the stagnation plate. Incipient particles grow by coagulation and surface growth forming partially sintered aggregates. The sintering level distribution shows a peak at 1.0 corresponding to spherical particles, indicating that inception continues well into the post-flame region. Fringe length distributions show a peak at about 1 nm, with lengths ranging from 1–6 nm. The largest fringe length in either distribution corresponds to a PAH which starts growing from just above the burner surface. Fringe lengths at point E are on average larger than at point D because the residence time between these two points is relatively long. The computed fringe length distributions compare favourably with experimental observations made for a range of fuels [66].

If indeed the soot particles were spherical, no benefit would be gained from tracking the aggregate structure of the particles. However, HIM of nascent soot particles for a number of premixed ethylene BSSF show that these particles are neither spherical nor chain-like [55, 56]. By imposing two different combinations of model parameters which result in two distinct soot morphologies this may help us to better interpret the mobility

diameter. First of all, based on the parameters in Table 1, the model allows for the formation of polydisperse, sintered primary particles which is shown as the dashed-dotted-dashed line in Fig. 10. An infinitely fast sintering rate (large $d_{\text{crit}}$) and the instantaneous rounding of primary particles (s = 0) results in spherical particles. This model represents an oversimplification and results in an underprediction of the diameter associated with the coagulation peak (as indicated by the circles). Extending the basic spherical particle model to a surface-volume model by neglecting the sintering process and not accounting for the rounding of primary particles ($s = 2$) results in an overprediction of the diameter. Unsurprising, there is little to no change in the position of the inception peak. It represents incipient particles which are spherical and all particle models effectively reduce to the spherical particle model. Menz and Kraft [40] demonstrated that under certain conditions, albeit in silica and silicon systems, all three models were equivalent to a spherical particle model. However, outside of this range, the spherical and surface-volume particle models were shown to incur substantial errors. In summary, this case study demonstrates that the prediction of the PSDs of an ensemble of polydisperse particles is dependent on the choice of the particle model. Where coagulation and sintering are significant the system is poorly described by spherical or surface-volume models.

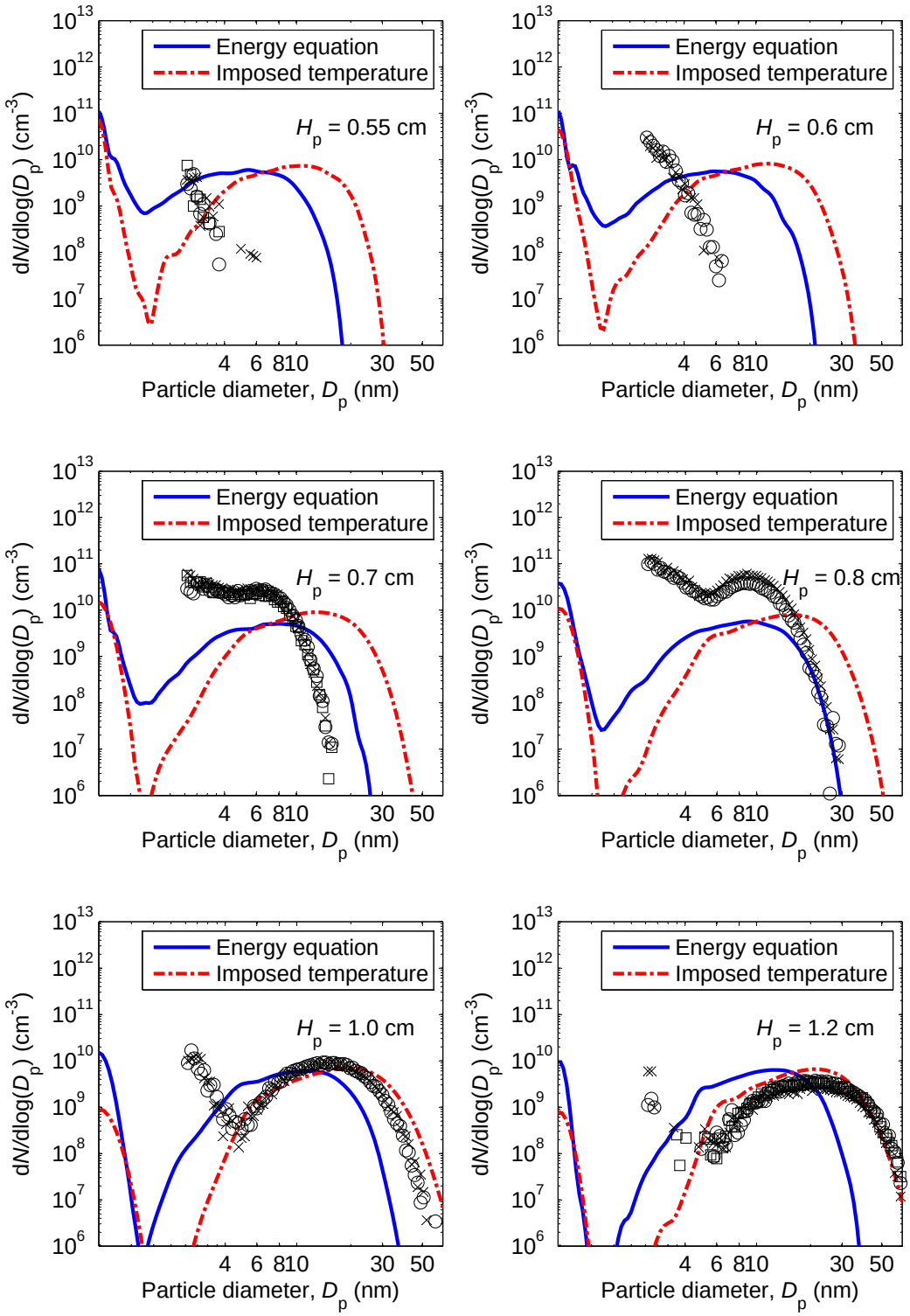


**Figure 6:** *Comparison of computed PSDs where the energy equation was solved (solid line) and where the experimental temperature profile was imposed (dashed-dotted-dashed line) at several burner-stagnation plate separations. Symbols are experimental data. Different symbols are used for different repeat experiments.*

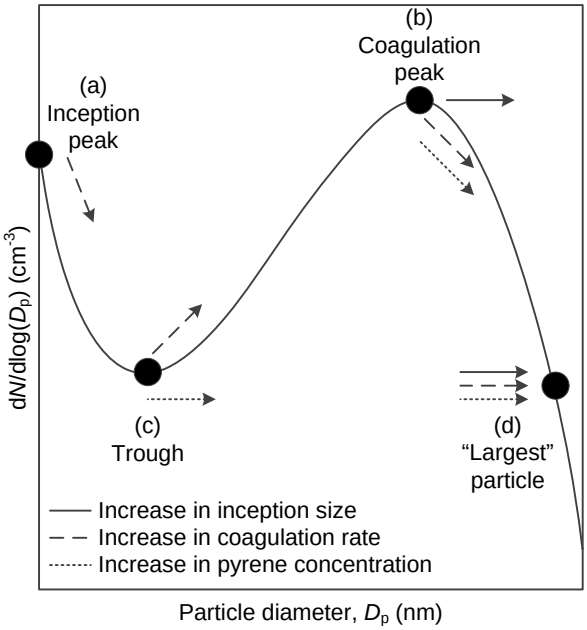


**Figure 7:** *Features of a bimodal PSD and summary of effects of the model parameters tested on the key features of the PSD.*

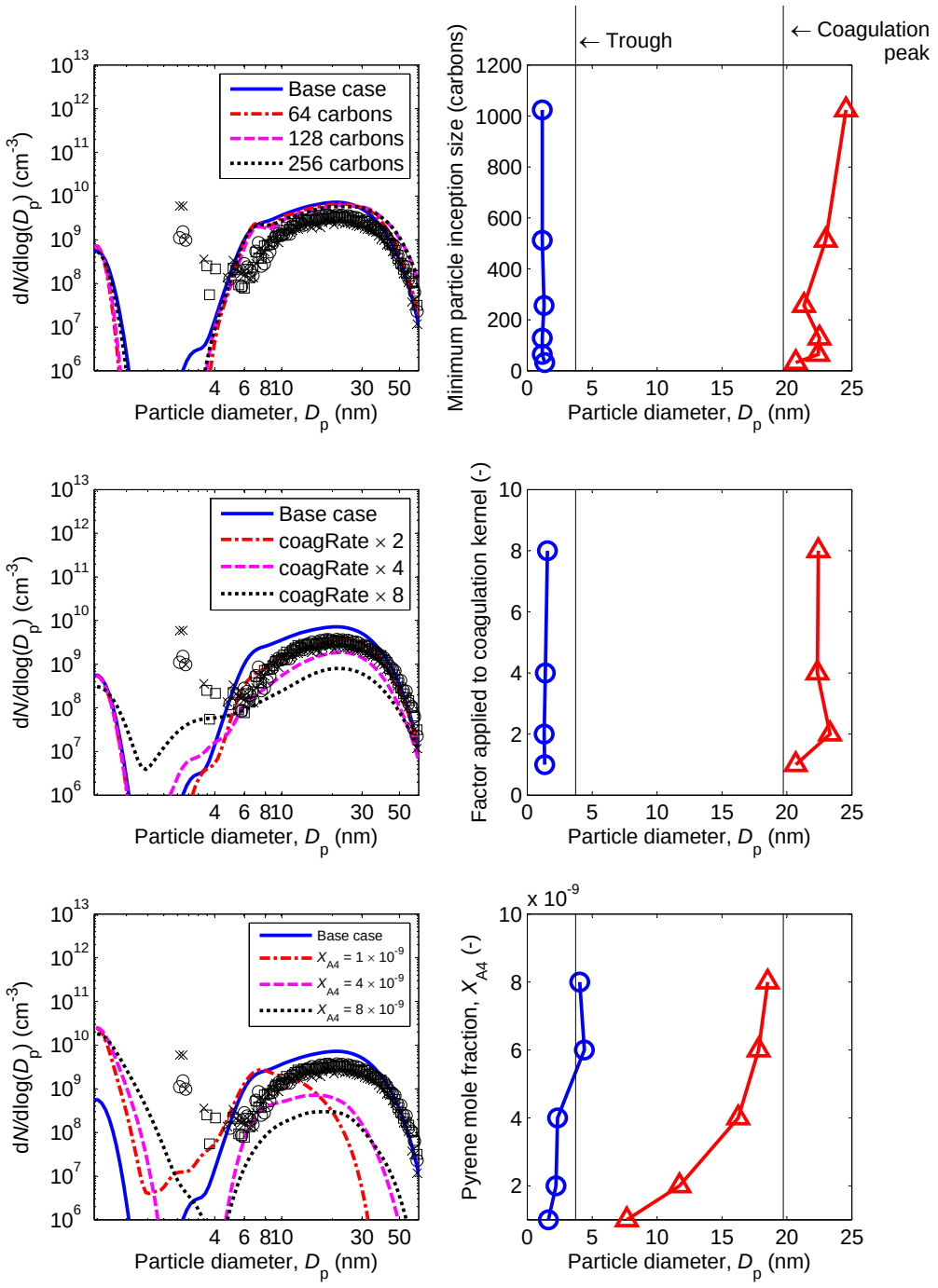


**Figure 8:** *Sensitivity of computed (lines) PSDs to the minimum particle inception size (top panel), the coagulation rate (middle panel) and the pyrene concentration (bottom panel) for a burner-stagnation plate separation of 1.2 cm where the experimental temperature profile was imposed. Left column: Symbols are experimental data. Different symbols are used for different repeat experiments. Right column: Sensitivity of the position of the trough between the modes of the bimodal PSD (circles) and the position of the coagulation peak (triangles). The vertical lines correspond to the experimental values for the trough (point c of Figure 7) and coagulation peak (point b of Figure 7).*

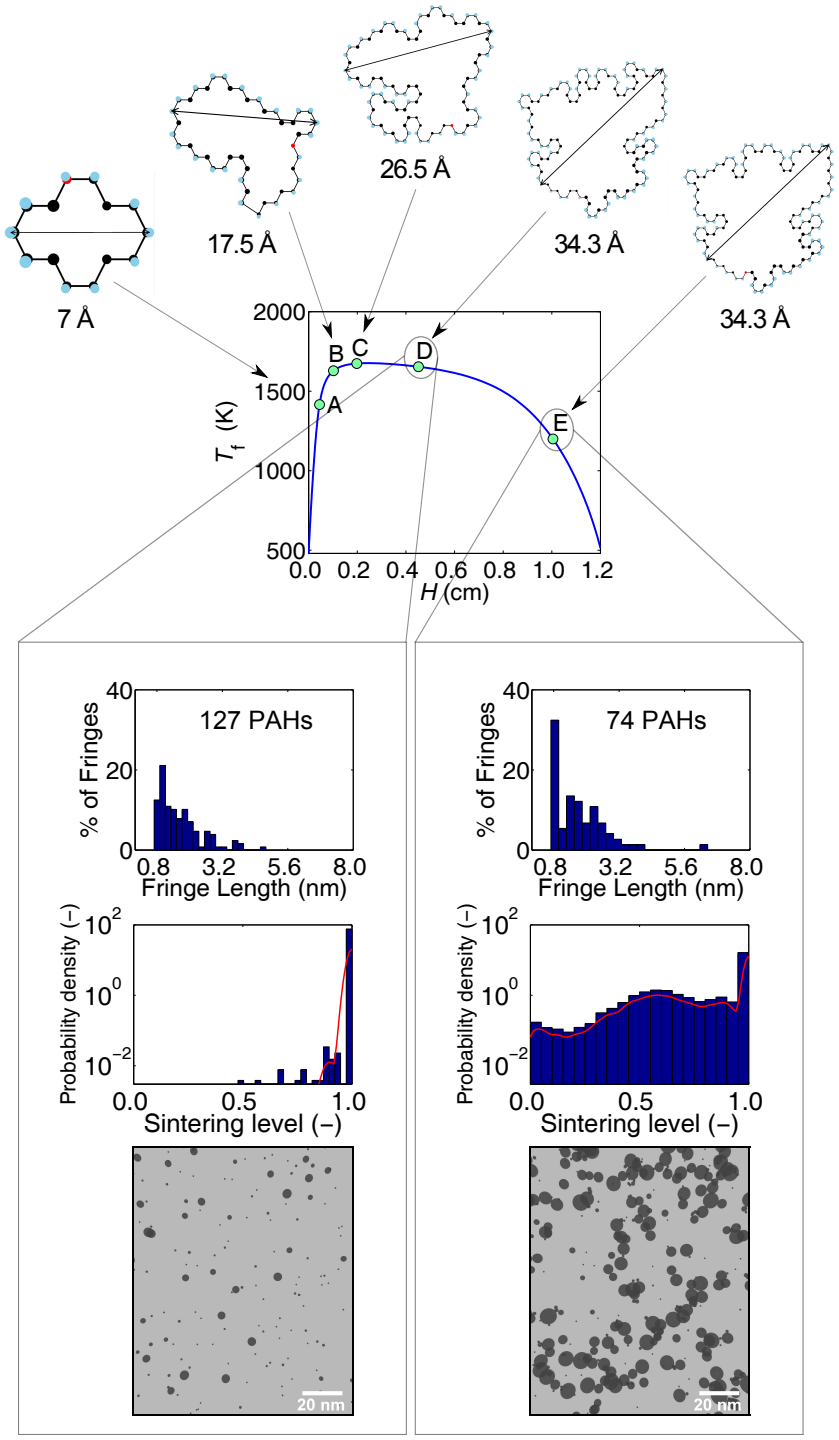


**Figure 9:** *Top panel: Evolution of the structure and fringe length of a representative PAH corresponding to points A–E on the temperature profile. Bottom panel (starting from the top): Fringe length distributions (the number of PAHs in the aggregate is shown), sintering level distributions and TEM images corresponding to points D and E on the temperature profile.*

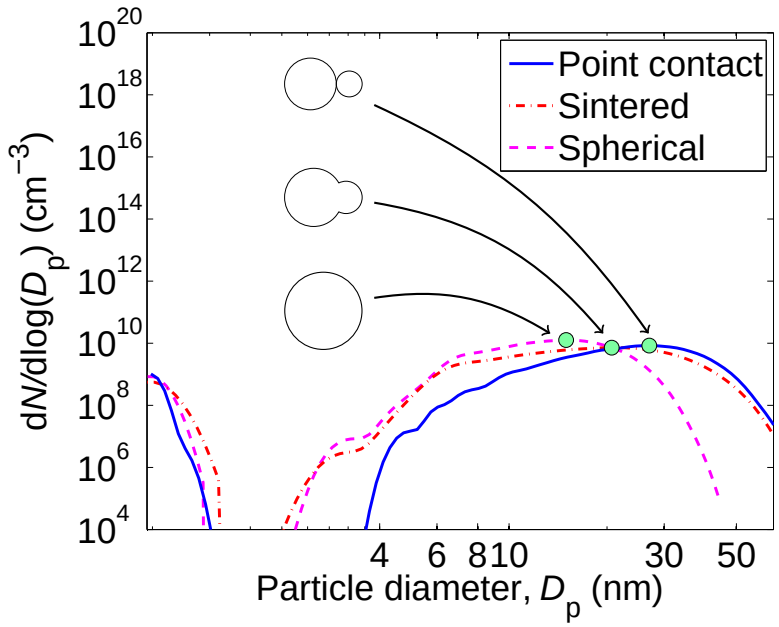


**Figure 10:** *Computed PSDs for a burner-stagnation plate separation of 1.2 cm with imposed experimental temperature profile for three different model cases: 1) polydisperse, spherical primary particles in point contact, 2) polydisperse, sintered primary particles and 3) spherical particles. The circles indicate the position of the coagulation peak.*

# 4 Implication on Mobility Sizing Experiments

Simulations carried out here cast some doubts about the accuracy of experimental data of Flame C3 [4]. Clearly, the exhaustive sensitivity analyses show that within the framework of the current model it would be difficult to reconcile the detailed features of the measured PSDs across all burner-probe separations and within a PSD from small to large particle sizes. There are several experimental issues that will require further scrutiny. First, the drastically different PSDFs for small burner-probe separations (see, Fig. 6) require the experiments to be revisited and repeated, especially to make sure that there is no facility/burner-dependent issues involved in the original measurement. The discrepancy in the trough position can be a problem of mobility data interpretation. For small particle sizes, the diffusional loss in the differential mobility size and its manufacturer-defined correction can be a source of problem. Interpretation of the mobility size for ultra small particles and diffusional broadening of these particles can result in the shallow trough observed as compared to the computed results. Repeated measurements across several facilities and burner setups will be required to shed light on the problems discussed herein.

# 5 Conclusions

In this paper we have presented a modelling study of soot formation for a laminar premixed ethylene BSSF. A detailed population balance model was used to perform a parametric sensitivity study to understand the influence of the most important parameters on key features of the computed PSDs. We provided insight into soot formation through the analysis of computed sintering level distributions, fringe length distributions and TEM images.

The computed flame structure captured the trends in the experimental data, with temperatures reaching a maximum just above the burner surface. The computed minor species profiles were remarkably similar up to about 0.2 cm above the burner surface. The length of the post-flame region increases with increasing burner-stagnation plate separation.

We have illustrated a dependence of soot morphology upon flame conditions in the post-flame region. The computed particles are initially spherical, evolving to partially sintered aggregates. Computed fringe length distributions compare favourably with experimental distributions reported in the literature, with lengths ranging from 1–6 nm.

The base case simulations resulted in PSDs which overpredicted particle diameters at smaller separations and underpredicted particle diameters at larger separations. A parametric sensitivity study was performed to understand the cause of the discrepancies between the experimental and computed PSDs. The computed PSDs were found to be most sensitive to the minimum particle inception size, the coagulation rate and the inception species concentration. The PSDs were generally insensitive to the other parameters in the population balance model. Changes in the particle inception size and the coagulation rate led to an overall shift in the position of the coagulation peak. Only changes in the inception species concentration led to a systematic shift in both the position of the trough between the modes of the bimodal PSD and the coagulation peak at larger diam-

eters. Given the overall model, varying the inception species concentration with each burner-stagnation plate separation was the only means possible of achieving a satisfactory agreement between the experimental and computed PSDs and soot volume fractions. The fact that the experimental PSDs cannot be reconciled by the model within its current frame work suggests (i) the experiment will have to be reproduced, and/or (ii) a better understanding of the nucleation process, including the PAH precursor chemistry, is required before further progress can be made.

# Acknowledgements

Discussions with Professor M. J. Thomson, Dr. W. J. Menz and Mr. A. J. Smith were helpful in the direction of this work. Financial support by the Gates Cambridge is gratefully acknowledged. This project is partly funded by the National Research Foundation (NRF), Prime Minister's Office, Singapore under its Campus for Research Excellence and Technological Enterprise (CREATE) programme. Professor Markus Kraft has been supported by the Weierstrass Institute for Applied Analysis and Stochastics.

# Nomenclature

**Greek**

$\alpha_T$ Thermal accommodation factor (-), see Eq. (12)
$\kappa$ Planck mean absorption coefficient of a soot particle ($m^{-1}$), see Eq. (8)
$\Lambda$ Radial pressure gradient eigenvalue ($kg\,m^{-3}\,s^{-2}$), see Eq. (3)
$\lambda$ Thermal conductivity ($kg\,m\,s^{-3}\,K^{-1}$), see Eq. (7)
$\mu$ Dynamic viscosity ($kg\,m^{-1}\,s^{-1}$), see Eq. (3)
$v_r$ Radial velocity ($m\,s^{-1}$), see Eq. (2)
$v_T$ Thermophoretic velocity ($m\,s^{-1}$), see Eq. (13)
$\dot{\omega}$ Molar chemical rate of production per unit volume ($mol\,m^{-3}\,s^{-1}$), see Eq. (5)
$\phi$ Dependent variable vector
$\rho$ Density ($kg\,m^{-3}$), see Eq. (2)
$\sigma$ Stefan-Boltzmann constant ($kg\,s^{-3}\,K^{-4}$), see Eq. (8)
$\tau_s$ Sintering time (s), see Eq. (19)

**Mathematical notations**

$\bar{x}$ Mean (-), see Eq. (6)
$\dot{x}$ Time derivative, see Eq. (10)

**Lower-case Roman**

$a$ Planck mean absorption coefficient of a gas-phase species ($s^2\,kg^{-1}$), see Eq. (8)
$c$ Sintering level (-)
$c_p$ Specific heat capacity at constant pressure ($m^2\,s^{-2}\,K^{-1}$), see Eq. (7)
$d$ Diameter (m), see Eq. (12)
$f_v$ Soot volume fraction (-), see Eq. (9)
$g$ Growth factor (-)
$h$ Molar enthalpy ($kg\,m^2\,s^{-2}\,mol^{-1}$), see Eq. (7)
$i$ Particle of size $i$ (-), see Eq. (11)
$k$ Absorptive index (-), see Eq. (9)
$k_B$ Boltzmann constant ($kg\,m^2\,s^{-2}\,K^{-1}$), see Eq. (12)
$n$ Number of primary particles (-), see Eq. (22)
$n$ Refractive index (-), see Eq. (9)
$n_{crit}$ Critical number of PAHs in a primary particle before the growth factor is applied (-)
$n_c$ Number of carbon atoms, see Eq. (21)
$p$ Pressure ($kg\,m^{-1}\,s^{-2}$), see Eq. (4)
$p$ Primary particle (-)
$r$ Radial distance (m), see Eq. (4)
$s$ Smoothing factor (-)
$u$ Axial velocity ($m\,s^{-1}$), see Eq. (2)
$z$ Axial distance (m), see Eq. (1)

**Subscripts**

| | |
|---|---|
| 1 | Particle of size 1, see Eq. (10) |
| amb | Ambient, see Eq. (8) |
| b | Burner, see Eq. (14) |
| crit | Critical, see Eq. (19) |
| c | Collision, see Eq. (21) |
| $k$ | Species index, see Eq. (5) |
| p | Particle, see Eq. (10) |
| p | Primary, see Eq. (22) |
| $r$ | Moment order, see Eq. (11) |
| s | Stagnation, see Eq. (16) |

**Upper-case Roman**

| | |
|---|---|
| $A$ | Area ($m^2$), see Eq. (22) |
| $A$ | Pre-exponential factor ($s\,m^{-1}$), see Eq. (19) |
| $C$ | Shared surface area between two neighbouring primary particles ($m^2$), see Eq. (18) |
| $C_0$ | Constant (-), see Eq. (9) |
| $C_2$ | Second Planck function constant ($m\,K$), see Eq. (9) |
| $D_p$ | Particle diameter (m) |
| $D_p$ | Particle diffusion coefficient ($m^2\,s^{-1}$), see Eq. (12) |
| $D_f$ | Fractal dimension (-), see Eq. (22) |
| $D_{k,j}$ | Multicomponent diffusion coefficient of the $k$-th species in species $j$ ($m^2\,s^{-1}$), see Eq. (6) |
| $D_{T,k}$ | Thermal diffusion coefficient of the $k$-th species ($kg\,m^{-1}\,s^{-1}$), see Eq. (6) |
| $E$ | Activation energy (K), see Eq. (19) |
| $F$ | Factor related to axial velocity ($kg\,m^{-2}\,s^{-1}$), see Eq. (1) |
| $G$ | Factor related to radial velocity ($kg\,m^{-3}\,s^{-1}$), see Eq. (1) |
| $H_p$ | Burner-stagnation plate separation (m), see Eq. (16) |
| $H$ | Height above burner surface (m) |
| $M$ | Moments of the size distribution of soot particles ($m^{-3}\,s^{-1}$), see Eq. (11) |
| $N$ | Number density ($m^{-3}$), see Eq. (11) |
| $N$ | Number of species (-), see Eq. (5) |
| $N_A$ | Avogadro constant ($mol^{-1}$), see Eq. (12) |
| $\dot{Q}_{rad}$ | Heat loss due to gas and particle radiation per unit volume ($kg\,m^{-1}\,s^{-3}$), see Eq. (7) |
| $S$ | Surface area of a sphere ($m^2$), see Eq. (18) |
| $T$ | Temperature (K), see Eq. (7) |
| $V$ | Diffusion velocity ($m\,s^{-1}$), see Eq. (5) |
| $V$ | Volume ($m^3$), see Eq. (21) |
| $W$ | Molecular weight ($kg\,mol^{-1}$), see Eq. (5) |
| $X$ | Mole fraction (-), see Eq. (6) |
| $Y$ | Mass fraction (-), see Eq. (5) |

# References


[1] CHEMKIN theory manual. CHEMKIN-PRO 15112, Reaction Design: San Diego, 2011.

[2] A. Abid, E. Tolmachoff, D. Phares, H. Wang, Y. Liu, and A. Laskin. Size distribution and morphology of nascent soot in premixed ethylene flames with and without benzene doping. *Proceedings of the Combustion Institute*, 32:681–688, 2009. doi:10.1016/j.proci.2008.07.023.

[3] A. D. Abid, N. Heinz, E. D. Tolmachoff, D. J. Phares, C. S. Campbell, and H. Wang. On evolution of particle size distribution functions of incipient soot in premixed ethylene–oxygen–argon flames. *Combustion and Flame*, 154:775–788, 2008. doi:10.1016/j.combustflame.2008.06.009.

[4] A. D. Abid, J. Camacho, D. A. Sheen, and H. Wang. Quantitative measurement of soot particle size distribution in premixed flames – the burner-stabilized stagnation flame approach. *Combustion and Flame*, 156:1862–1870, 2009. doi:10.1016/j.combustflame.2009.05.010.

[5] J. Akroyd, A. J. Smith, R. Shirley, L. R. McGlashan, and M. Kraft. A coupled CFD-population balance approach for nanoparticle synthesis in turbulent reacting flows. *Chemical Engineering Science*, 66:3792–3805, 2011. doi:10.1016/j.ces.2011.05.006.

[6] J. Appel, H. Bockhorn, and M. Frenklach. Kinetic modeling of soot formation with detailed chemistry and physics: laminar premixed flames of $C_2$ hydrocarbons. *Combustion and Flame*, 121:122–136, 2000. doi:10.1016/S0010-2180(99)00135-2.

[7] J. Bhatt and R. Lindstedt. Analysis of the impact of agglomeration and surface chemistry models on soot formation and oxidation. *Proceedings of the Combustion Institute*, 32:713–720, 2009. doi:10.1016/j.proci.2008.06.201.

[8] M. Celnik, R. Patterson, M. Kraft, and W. Wagner. Coupling a stochastic soot population balance to gas-phase chemistry using operator splitting. *Combustion and Flame*, 148:158–176, 2007. doi:10.1016/j.combustflame.2006.10.007.

[9] M. Celnik, A. Raj, R. West, R. Patterson, and M. Kraft. Aromatic site description of soot particles. *Combustion and Flame*, 155:161–180, 2008. doi:10.1016/j.combustflame.2008.04.011.

[10] M. Celnik, M. Sander, A. Raj, R. West, and M. Kraft. Modelling soot formation in a premixed flame using an aromatic-site soot model and an improved oxidation rate. *Proceedings of the Combustion Institute*, 32:639–646, 2009. doi:10.1016/j.proci.2008.06.062.

[11] D. Chen, Z. Zainuddin, E. Yapp, J. Akroyd, S. Mosbach, and M. Kraft. A fully coupled simulation of PAH and soot growth with a population balance model. *Proceedings of the Combustion Institute*, 34:1827–1835, 2013. doi:10.1016/j.proci.2012.06.089.

[12] M. Choi, G. Mulholland, A. Hamins, and T. Kashiwagi. Comparisons of the soot volume fraction using gravimetric and light extinction techniques. *Combustion and Flame*, 102:161–169, 1995. doi:10.1016/0010-2180(94)00282-W.

[13] A. D'Anna. Combustion-formed nanoparticles. *Proceedings of the Combustion Institute*, 32:593–613, 2009. doi:10.1016/j.proci.2008.09.005.

[14] L. Deng, A. Kempf, O. Korobeinichev, and I. Wlokas. Numerical investigation of the laminar flame perturbation by a sampling nozzle. *Paper presented at Poster Session (P2-24), European Combustion Meeting, Lund, Sweden*, 2013.

[15] R. Dobbins, R. Fletcher, and W. Lu. Laser microprobe analysis of soot precursor particles and carbonaceous soot. *Combustion and Flame*, 100:301–309, 1995. doi:10.1016/0010-2180(94)00047-V.

[16] R. Dobbins, R. Fletcher, and H.-C. Chang. The evolution of soot precursor particles in a diffusion flame. *Combustion and Flame*, 115:285–298, 1998. doi:10.1016/S0010-2180(98)00010-8.

[17] M. Frenklach. On surface growth mechanism of soot particles. *Symposium (International) on Combustion*, 26:2285–2293, 1996. doi:10.1016/S0082-0784(96)80056-7.

[18] M. Frenklach. Method of moments with interpolative closure. *Chemical Engineering Science*, 57:2229–2239, 2002. doi:10.1016/S0009-2509(02)00113-6.

[19] M. Frenklach and S. Harris. Aerosol dynamics modeling using the method of moments. *Journal of Colloid and Interface Science*, 118:252–261, 1987. doi:10.1016/0021-9797(87)90454-1.

[20] M. Frenklach and H. Wang. Detailed modeling of soot particle nucleation and growth. *Symposium (International) on Combustion*, 23:1559–1566, 1991. doi:10.1016/S0082-0784(06)80426-1.

[21] M. Frenklach and H. Wang. Detailed mechanism and modeling of soot particle formation. In H. Bockhorn (Ed.), *Soot formation in combustion-mechanisms and models* (pp. (165–190)). Berlin: Springer, 1994.

[22] M. Frenklach and J. Warnatz. Detailed modeling of PAH profiles in a sooting low-pressure acetylene flame. *Combustion Science and Technology*, 51:265–283, 1987. doi:10.1080/00102208708960325.

[23] S. Friedlander. *Smoke, dust, and haze*. New York: Oxford University Press, 2000.

[24] N. Fuchs. *The mechanics of aerosols*. New York: Dover, 1989.

[25] J. Happold. *Geschichtete polyzyklische aromatische kohlenwasserstoffe als bausteine der rußbildung*. PhD thesis, Universität Stuttgart, 2008.

[26] J. Hessler, S. Seifert, R. Winans, and T. Fletcher. Small-angle X-ray studies of soot inception and growth. *Faraday discussions*, pages 395–407; discussion 445–59, 2001.

[27] R. J. Kee, J. A. Miller, G. H. Evans, and G. Dixon-Lewis. A computational model of the structure and extinction of strained, opposed flow, premixed methane-air flames. *Symposium (International) on Combustion*, 22:1479–1494, 1989. doi:10.1016/S0082-0784(89)80158-4.

[28] U. Köylü, C. McEnally, D. Rosner, and L. Pfefferle. Simultaneous measurements of soot volume fraction and particle size / microstructure in flames using a thermophoretic sampling technique. *Combustion and Flame*, 110:494–507, 1997. doi:10.1016/S0010-2180(97)00089-8.

[29] F. E. Kruis, K. A. Kusters, S. E. Pratsinis, and B. Scarlett. A Simple Model for the Evolution of the Characteristics of Aggregate Particles Undergoing Coagulation and Sintering. *Aerosol Science and Technology*, 19:514–526, 1993. doi:10.1080/02786829308959656.

[30] P. Lavvas, M. Sander, M. Kraft, and H. Imanaka. Surface chemistry and particle shape: processes for the evolution of aerosols in titan's atmosphere. *The Astrophysical Journal*, 728:80, 2011. doi:10.1088/0004-637X/728/2/80.

[31] Z. Li and H. Wang. Drag force, diffusion coefficient, and electric mobility of small particles. I. Theory applicable to the free-molecule regime. *Physical Review E*, 68: 061206, 2003. doi:10.1103/PhysRevE.68.061206.

[32] Z. Li and H. Wang. Drag force, diffusion coefficient, and electric mobility of small particles. II. Application. *Physical Review E*, 68:061207, 2003. doi:10.1103/PhysRevE.68.061207.

[33] Z. Li and H. Wang. Thermophoretic force and velocity of nanoparticles in the free molecule regime. *Physical Review E*, 70:021205, 2004. doi:10.1103/PhysRevE.70.021205.

[34] R. Lindstedt and B. Waldheim. Modeling of soot particle size distributions in premixed stagnation flow flames. *Proceedings of the Combustion Institute*, 34:1861–1868, 2013. doi:10.1016/j.proci.2012.05.047.

[35] A. Lutz, R. Kee, J. Grear, and F. Rupley. OPPDIF: A Fortran program for computing opposed-flow diffusion flames. Sandia report SAND96-8243, UC-1409, 1997.

[36] M. Maricq. Size and charge of soot particles in rich premixed ethylene flames. *Combustion and Flame*, 137:340–350, 2004. doi:10.1016/j.combustflame.2004.01.013.

[37] M. M. Maricq. A comparison of soot size and charge distributions from ethane, ethylene, acetylene, and benzene/ethylene premixed flames. *Combustion and Flame*, 144:730–743, 2006. doi:10.1016/j.combustflame.2005.09.007.

[38] C. S. McEnally, U. O. Köylü, L. D. Pfefferle, and D. E. Rosner. Soot volume fraction and temperature measurements in laminar nonpremixed flames using thermocouples. *Combustion and Flame*, 109:701–720, 1997. doi:10.1016/S0010-2180(97)00054-0.

[39] R. Mehta, D. Haworth, and M. Modest. An assessment of gas-phase reaction mechanisms and soot models for laminar atmospheric-pressure ethylene-air flames. *Proceedings of the Combustion Institute*, 32:1327–1334, 2009. doi:10.1016/j.proci.2008.06.149.

[40] W. J. Menz and M. Kraft. The suitability of particle models in capturing aggregate structure and polydispersity. *Aerosol Science and Technology*, 47:734–745, 2013. doi:10.1080/02786826.2013.788244.

[41] W. J. Menz and M. Kraft. A new model for silicon nanoparticle synthesis. *Combustion and Flame*, 160:947–958, 2013. doi:10.1016/j.combustflame.2013.01.014.

[42] M. Modest. *Radiative heat transfer*. Chemical, Petrochemical & Process. Sand Diego: Academic Press, 2003.

[43] N. Morgan, M. Kraft, M. Balthasar, D. Wong, M. Frenklach, and P. Mitchell. Numerical simulations of soot aggregation in premixed laminar flames. *Proceedings of the Combustion Institute*, 31:693–700, 2007. doi:10.1016/j.proci.2006.08.021.

[44] S. Mosbach, M. S. Celnik, A. Raj, M. Kraft, H. R. Zhang, S. Kubo, and K.-O. Kim. Towards a detailed soot model for internal combustion engines. *Combustion and Flame*, 156:1156–1165, 2009. doi:10.1016/j.combustflame.2009.01.003.

[45] B. Öktem, M. P. Tolocka, B. Zhao, H. Wang, and M. V. Johnston. Chemical species associated with the early stage of soot growth in a laminar premixed ethylene–oxygen–argon flame. *Combustion and Flame*, 142:364–373, 2005. doi:10.1016/j.combustflame.2005.03.016.

[46] R. I. Patterson, J. Singh, M. Balthasar, M. Kraft, and W. Wagner. Extending stochastic soot simulation to higher pressures. *Combustion and Flame*, 145:638–642, 2006. doi:10.1016/j.combustflame.2006.02.005.

[47] H. Pitsch, E. Riesmeier, and N. Peters. Unsteady flamelet modeling of soot formation in turbulent diffusion flames. *Combustion Science and Technology*, 158: 389–406, 2000. doi:10.1080/00102200008947342.

[48] R. Puri, R. J. Santoro, and K. C. Smyth. The oxidation of soot and carbon monoxide in hydrocarbon diffusion flames. *Combustion and Flame*, 97:125–144, 1994. doi:10.1016/0010-2180(94)90001-9.

[49] A. Raj, M. Celnik, R. Shirley, M. Sander, R. Patterson, R. West, and M. Kraft. A statistical approach to develop a detailed soot growth model using PAH characteristics. *Combustion and Flame*, 156:896–913, 2009. doi:10.1016/j.combustflame.2009.01.005.

[50] A. Raj, P. L. Man, T. S. Totton, M. Sander, R. A. Shirley, and M. Kraft. New polycyclic aromatic hydrocarbon (PAH) surface processes to improve the model prediction of the composition of combustion-generated PAHs and soot. *Carbon*, 48: 319–332, 2010. doi:10.1016/j.carbon.2009.09.030.

[51] A. Raj, M. Sander, V. Janardhanan, and M. Kraft. A study on the coagulation of polycyclic aromatic hydrocarbon clusters to determine their collision efficiency. *Combustion and Flame*, 157:523–534, 2010. doi:10.1016/j.combustflame.2009.10.003.

[52] K. L. Revzan, N. J. Brown, and M. Frenklach. Soot formation codes, 1999. URL `http://www.me.berkeley.edu/soot`.

[53] M. Sander, R. H. West, M. S. Celnik, and M. Kraft. A detailed model for the sintering of polydispersed nanoparticle agglomerates. *Aerosol Science and Technology*, 43: 978–989, 2009. doi:10.1080/02786820903092416.

[54] M. Sander, R. I. Patterson, A. Braumann, A. Raj, and M. Kraft. Developing the PAH-PP soot particle model using process informatics and uncertainty propagation. *Proceedings of the Combustion Institute*, 33:675–683, 2011. doi:10.1016/j.proci.2010.06.156.

[55] M. Schenk, S. Lieb, H. Vieker, A. Beyer, A. Gölzhäuser, H. Wang, and K. Kohse-Höinghaus. Imaging Nanocarbon Materials: Soot Particles in Flames are Not Structurally Homogeneous. *Chemphyschem : a European journal of chemical physics and physical chemistry*, 14:3248–3254, 2013. doi:10.1002/cphc.201300581.

[56] M. Schenk, S. Lieb, H. Vieker, A. Beyer, A. Gölzhäuserc, H. Wang, and K. Kohse-Höinghaus. Morphology of nascent soot in ethylene flames. *Proceedings of the Combustion Institute*, in press, 2014. doi:10.1016/j.proci.2014.05.009.

[57] J. Seinfeld and S. Pandis. *Atmospheric chemistry and physics. From air pollution to climate change*. New York: Wiley, 1998.

[58] L. Sgro, A. De Filippo, G. Lanzuolo, and A. D'Alessio. Characterization of nanoparticles of organic carbon (NOC) produced in rich premixed flames by differential mobility analysis. *Proceedings of the Combustion Institute*, 31:631–638, 2007. doi:10.1016/j.proci.2006.08.026.

[59] C. R. Shaddix and K. C. Smyth. Laser-induced incandescence measurements of soot production in steady and flickering methane, propane, and ethylene diffusion flames. *Combustion and Flame*, 107:418–452, 1996. doi:10.1016/S0010-2180(96)00107-1.

[60] R. Siegel and J. R. Howell. *Thermal radiation heat transfer*. New York: Hemisphere Publishing Corporation, 1981.

[61] J. Singh, M. Balthasar, M. Kraft, and W. Wagner. Stochastic modeling of soot particle size and age distributions in laminar premixed flames. *Proceedings of the Combustion Institute*, 30:1457–1465, 2005. doi:10.1016/j.proci.2004.08.120.

[62] J. Singh, R. I. Patterson, M. Kraft, and H. Wang. Numerical simulation and sensitivity analysis of detailed soot particle size distribution in laminar premixed ethylene flames. *Combustion and Flame*, 145:117–127, 2006. doi:10.1016/j.combustflame.2005.11.003.

[63] M. Smooke, I. Puri, and K. Seshadri. A comparison between numerical calculations and experimental measurements of the structure of a counterflow diffusion flame burning diluted methane in diluted air. *Symposium (International) on Combustion*, 21:1783–1792, 1988. doi:10.1016/S0082-0784(88)80412-0.

[64] K. C. Smyth and C. R. Shaddix. The elusive history of $\tilde{m} = 1.57 - 0.56i$ for the refractive index of soot. *Combustion and Flame*, 107:314–320, 1996. doi:10.1016/S0010-2180(96)00170-8.

[65] S. Tsantilis, H. Briesen, and S. Pratsinis. Sintering time for silica particle growth. *Aerosol Science and Technology*, 34:237–246, 2001. doi:10.1080/02786820119149.

[66] R. L. Vander Wal and A. J. Tomasek. Soot oxidation. *Combustion and Flame*, 134: 1–9, 2003. doi:10.1016/S0010-2180(03)00084-1.

[67] L. Waldmann and K. Schmitt. Thermophoresis and Diffusiophoresis of Aerosols. In C. N. Davies (Ed.), *Aerosol Science* (pp. (137–162)). London: Academic Press, 1966.

[68] H. Wang. Formation of nascent soot and other condensed-phase materials in flames. *Proceedings of the Combustion Institute*, 33:41–67, 2011. doi:10.1016/j.proci.2010.09.009.

[69] H. Wang and M. Frenklach. A detailed kinetic modeling study of aromatics formation in laminar premixed acetylene and ethylene flames. *Combustion and Flame*, 110:173–221, 1997. doi:10.1016/S0010-2180(97)00068-0.

[70] H. Wang, D. Du, C. Sung, and C. Law. Experiments and numerical simulation on soot formation in opposed-jet ethylene diffusion flames. *Symposium (International) on Combustion*, 26:2359–2368, 1996. doi:10.1016/S0082-0784(96)80065-8.

[71] H. Wang, B. Zhao, B. Wyslouzil, and K. Streletzky. Small-angle neutron scattering of soot formed in laminar premixed ethylene flames. *Proceedings of the Combustion Institute*, 29:2749–2757, 2002. doi:10.1016/S1540-7489(02)80335-2.

[72] H. Wang, X. You, A. Joshi, S. Davis, A. Laskin, F. Egolfopoulos, and C. Law. USC Mech Version II. High-temperature combustion reaction model of $H_2/CO/C_1 - C_4$ compounds, 2007. URL `http://ignis.usc.edu/USC_Mech_II.htm/`.

[73] R. H. West, R. A. Shirley, M. Kraft, C. F. Goldsmith, and W. H. Green. A detailed kinetic model for combustion synthesis of titania from $TiCl_4$. *Combustion and Flame*, 156:1764–1770, 2009. doi:10.1016/j.combustflame.2009.04.011.

[74] B. Zhao, Z. Yang, M. V. Johnston, H. Wang, A. S. Wexler, M. Balthasar, and M. Kraft. Measurement and numerical simulation of soot particle size distribution functions in a laminar premixed ethylene-oxygen-argon flame. *Combustion and Flame*, 133:173–188, 2003. doi:10.1016/S0010-2180(02)00574-6.

[75] B. Zhao, Z. Yang, J. Wang, M. V. Johnston, and H. Wang. Analysis of soot nanoparticles in a laminar premixed ethylene flame by scanning mobility particle sizer. *Aerosol Science and Technology*, 37:611–620, 2003. doi:10.1080/02786820300908.

[76] B. Zhao, Z. Yang, Z. Li, M. V. Johnston, and H. Wang. Particle size distribution function of incipient soot in laminar premixed ethylene flames: effect of flame temperature. *Proceedings of the Combustion Institute*, 30:1441–1448, 2005. doi:10.1016/j.proci.2004.08.104.

[77] B. Zhao, K. Uchikawa, and H. Wang. A comparative study of nanoparticles in premixed flames by scanning mobility particle sizer, small angle neutron scattering, and transmission electron microscopy. *Proceedings of the Combustion Institute*, 31: 851–860, 2007. doi:10.1016/j.proci.2006.08.064.